PHYSICS OF FLUIDS **27**, 092002 (2015)

Self-electrophoresis of spheroidal electrocatalytic swimmers

Amir Nourhani,[1,2,a)] Vincent H. Crespi,[2,3,4] Paul E. Lammert,[2] and Ali Borhan[1]

[1]*Department of Chemical Engineering, The Pennsylvania State University, University Park, Pennsylvania 16802, USA*
[2]*Department of Physics, The Pennsylvania State University, University Park, Pennsylvania 16802, USA*
[3]*Department of Materials Science and Engineering, The Pennsylvania State University, University Park, Pennsylvania 16802, USA*
[4]*Department of Chemistry, The Pennsylvania State University, University Park, Pennsylvania 16802,USA*

(Received 22 March 2015; accepted 8 August 2015; published online 24 September 2015)

Using the method of matched asymptotic expansions, we derive a general expression for the speed of a prolate spheroidal electrocatalytic nanomotor in terms of interfacial potential and physical properties of the motor environment in the limit of small Debye length and Péclet number. This greatly increases the range of geometries that can be handled without resorting to numerical simulations, since a wide range of shapes from spherical to needle-like, and in particular the common cylindrical shape, can be well-approximated by prolate spheroids. For piecewise-uniform distribution of surface cation flux with fixed average absolute value, the mobility of a prolate spheroidal motor with a symmetric cation source/sink configuration is a monotonically decreasing function of eccentricity. A prolate spheroidal motor with an asymmetric sink/source configuration moves faster than its symmetric counterpart and can exhibit a non-monotonic dependence of motor speed on eccentricity for a highly asymmetric design. © *2015 AIP Publishing LLC.* [http://dx.doi.org/10.1063/1.4929518]

I. INTRODUCTION

In the growing field of active swimmers and micro- and nanomotors,[1–20] electrocatalytic designs[21–31] have had a prominent place. Improvements have led to higher speeds,[32–34] magnetic steering,[35,36] and cargo-carrying capabilities.[36,37] These swimmers self-propel by harvesting chemical free energy from their environments and transducing it to mechanical energy via *self-electrophoresis*.[23–31] An operating electrocatalytic motor is essentially an inside-out electrochemical cell with half-reactions occurring asymmetrically over the surface, leading to a heterogeneous surface cation flux. In the example shown in Fig. 1 of a platinum/gold bimetallic nanorod in hydrogen peroxide, hydrogen ions are predominantly produced over the platinum side by the anodic half-reaction and consumed over the gold side by the cathodic half-reaction, sustaining an asymmetric stationary nonequilibrium cloud of ions around the nanomotor and a nonequilibrium electric field which drives currents of reactive cations (and spectator ions) around the motor. These ions act as the motor's "oars," mediating a body force and thence an electrokinetic flow around the motor. This rough explanation of the motive mechanism of such motors received strong early support from experiments[26] which showed that, for a variety of metal combinations, a motor moves with the lower mixed potential (anodic) end forward and its speed increases as the difference of mixed potential between the constituent metals increases.

Quantitative analysis leading to an expression for self-electrophoretic speed in the limit of thin Debye layer was pioneered by Yariv[28] and later advanced by Sabass and Seifert[29] using

a)Electronic mail: nourhani@psu.edu

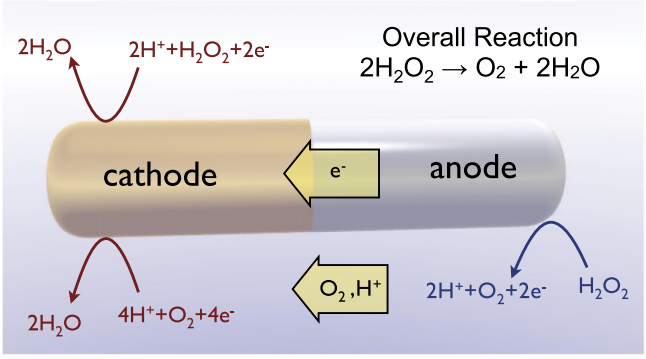

FIG. 1. Electrocatalytic decomposition of hydrogen peroxide produces hydrogen cations at the anode surface and consumes them at the cathode, yielding an asymmetric ion distribution in the motor vicinity.

Butler-Volmer kinetics, while Moran and Posner treated the problem numerically.[38] Nourhani *et al.*[23,24] worked from a general distribution of cation flux over a spherical motor surface and showed that in the linear regime, only the first Legendre coefficient of that flux contributes to motor speed. Specification of the flux may, but need not,[30,31] come from a chemical kinetics calculation. To date, theoretical studies of electrocatalytic swimmers have been specialized to spheres,[23,28,29] slender bodies,[28] or rods;[30,31] a systematic analysis that demonstrates the dependence of motor speed on shape is lacking. In this paper, we extend our previous matched-asymptotics analysis[23] for spherical motors to the case of prolate spheroids with a general axisymmetric cation flux distribution. Since a wide range of shapes—from spherical to rod-like—can be well-approximated as prolate spheroids by varying the eccentricity, this unification provides a basis for understanding shape dependence of motor performance.

The physical phenomena involved in self-electrophoresis have much in common with the migration of metallic or dielectric colloids driven through an electrolyte by weak external fields, a well-established subject with a long history.[39–45] A similar framework can be employed for electrocatalytic swimmers.[23,28,29] From this perspective, the peculiarities of these motors are a driving force generated by reactions on the motor surface rather than supplied externally and a non-zero flux $\boldsymbol{J}_+$ of reactive cations at the motor surface. One effective approach for rigorous analyses of this kind of electrokinetic problem is the method of matched asymptotic expansions in the limit of thin electrical double layer, where the motor's linear dimensions are much larger than the Debye length,

$$\lambda_D \equiv \sqrt{\frac{\epsilon\,\phi_T}{2zFC_+^\infty}}, \tag{1}$$

which is typically about 0.2 μm in experimental realizations and is determined by the permittivity ϵ of the fluid, the thermal potential $\phi_T \equiv RT/(zF)$ ($\approx$25 mV for monovalent cations at room temperature), the universal gas constant R, the absolute temperature T, Faraday's constant F, the ionic valence z of the cation, and the far-field concentrations of the reactive cation C_+^∞. In Section II, we describe the problem formulation for self-electrophoresis of a prolate spheroidal swimmer. In Section III, we obtain an expression (37) for the motor speed to leading order in the dimensionless Debye length $\lambda = \lambda_D/a$ and the dimensionless average absolute cation flux [see Eq. (7) below]. In Section IV, we interpret experimental results from the literature based on the main result of Section III and examine the effect of geometry for nanomotors with piecewise-uniform flux distribution. We conclude with a discussion of results in Section V.

II. PROBLEM FORMULATION

The nanomotor surface is modelled as prolate spheroid $(x^2 + y^2)/b^2 + z^2/a^2 = 1$, with semi-major axis a, semi-minor axis b, and eccentricity $0 \le \varepsilon \equiv \sqrt{1 - b^2/a^2} < 1$. As the eccentricity

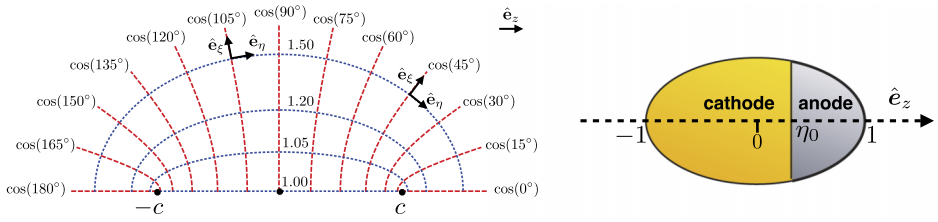

FIG. 2. Left: Prolate spheroidal coordinates on a plane containing the z-axis. The blue ellipses are loci of constant ξ, the red curves are loci of constant η, and the points at $\pm c = \pm\varepsilon a$ along the z axis are common foci of all constant-ξ ellipsoids. Right: Schematic of a prolate spheroidal nanomotor with axisymmetric position-dependent surface distributions of cation flux over the cation source (anode) and sink (cathode) regions designated by $\eta > \eta_0$ and $\eta < \eta_0$, respectively.

is varied, a prolate spheroid approximates a range of shapes, from a sphere ($\varepsilon = 0$) to axisymmetric slender bodies and rods [$(1-\varepsilon) \ll 1$]. Prolate spheroidal coordinates are a convenient choice in this situation, as in prior calculations of the self-propelling speed in Marangoni-driven systems.[46] In this coordinate system (illustrated in Fig. 2), each point is represented by a tuple $(\xi, \eta\ \varphi) \in [1,\infty) \times [-1,1] \times [0,2\pi)$ which can be translated to Cartesian coordinates using length scale a according to

$$(x/a, y/a, z/a) = \left(g_3^{-1}\cos\varphi, g_3^{-1}\sin\varphi, \varepsilon\xi\eta\right), \tag{2}$$

where g_3 is among the metric factors,

$$g_1(\xi,\eta) = \frac{1}{\varepsilon}\sqrt{\frac{\xi^2-1}{\xi^2-\eta^2}}, \qquad g_2(\xi,\eta) = \frac{1}{\varepsilon}\sqrt{\frac{1-\eta^2}{\xi^2-\eta^2}}, \qquad g_3(\xi,\eta) = \frac{1}{\varepsilon\sqrt{(\xi^2-1)(1-\eta^2)}}, \tag{3}$$

which enter the formulas for line "ds," area "dA," and volume "dV" elements,

$$\left(\frac{ds}{a}\right)^2 = \frac{d\xi^2}{g_1^2} + \frac{d\eta^2}{g_2^2} + \frac{d\varphi^2}{g_3^2}, \qquad \frac{dA}{a^2}\Big|_\xi = \frac{d\eta\, d\varphi}{g_2 g_3} = \frac{1-\varepsilon^2}{\varepsilon g_1}\, d\eta\, d\varphi, \qquad \frac{dV}{a^3} = \frac{d\xi\, d\eta\, d\varphi}{g_1 g_2 g_3}. \tag{4}$$

The surface $\xi = \xi_s (\equiv \varepsilon^{-1})$ is a spheroid with semi-major axis a, eccentricity ε, and area

$$A = 2\pi a^2\left[(1-\varepsilon^2) + \sqrt{1-\varepsilon^2}\,\frac{\sin^{-1}\varepsilon}{\varepsilon}\right]. \tag{5}$$

The factorized choice of scale factor in the translation to Cartesian coordinates allows us to easily think about varying a and ε independently. The actions of the gradient and Laplacian on axisymmetric (φ-independent) functions are given in spheroidal coordinates by

$$a\boldsymbol{\nabla} f(\xi,\eta) = \hat{\mathbf{e}}_\xi g_1\,\partial_\xi f + \hat{\mathbf{e}}_\eta g_2\,\partial_\eta f, \tag{6a}$$

$$a^2\nabla^2 f(\xi,\eta) = \frac{1}{\varepsilon^2(\xi^2-\eta^2)}\Big(\partial_\xi\left[(\xi^2-1)\partial_\xi f\right] + \partial_\eta\left[(1-\eta^2)\partial_\eta f\right]\Big), \tag{6b}$$

with $\hat{\mathbf{e}}_\xi$ and $\hat{\mathbf{e}}_\eta$ denoting the unit vectors in the ξ and η directions, respectively, as shown in Fig. 2. Expression (6b) reflects separability of the Laplace equation in spheroidal coordinates.

We model the fluid as a symmetric binary electrolyte of reactive cations (+) and passive anions (−) with absolute ionic valence $z \equiv z_+ = -z_-$. The physical properties of the fluid, such as viscosity μ and permittivity ϵ, are assumed uniform in space. As in Ref. 23, all quantities are made dimensionless using the characteristic scales shown in Table I; the dimensionless version of quantity G is written with an undertilde, e.g., "$\underset{\sim}{G}$."

Reactive cations are produced and consumed over the motor surface S, with an axisymmetric cation flux distribution $\hat{n}\cdot\underset{\sim}{\boldsymbol{J}}_+$ that is a function only of η. A suitable measure of the intensity of catalytic activity is the average absolute cation flux, $\underset{\sim}{j}_+$, defined as

$$\underset{\sim}{j}_+ = \frac{1}{\underset{\sim}{A}}\int_S |\hat{n}\cdot\underset{\sim}{\boldsymbol{J}}_+|\, d\underset{\sim}{A}. \tag{7}$$

TABLE I. The characteristic scales used in making field variables dimensionless.

Variable	Scale
Length	a (semi-major axis)
Velocity	$\epsilon\phi_T^2/\mu a$
Pressure	$\epsilon\phi_T^2/a^2$
Stress	$\epsilon\phi_T^2/a^2$
Electric potential	ϕ_T (thermal potential)
Concentration	C_+^∞ (far-field cation concentration)
Flux	$D_{\min}C_+^\infty/a$, where $D_{\min} \equiv \min(D_+, D_-)$

The surface cation flux distribution is thus written in the form

$$\hat{n} \cdot \underset{\sim}{\boldsymbol{J}}_+\big|_S = \underset{\sim}{j}_+ f(\eta), \tag{8}$$

where the $O(1)$ distribution function $f(\eta)$ represents the heterogeneity of surface cation flux and satisfies the constraints,

$$\int_S f(\eta)\, d\underset{\sim}{A} = 0, \qquad \frac{1}{\underset{\sim}{A}} \int_S |f(\eta)|\, d\underset{\sim}{A} = 1. \tag{9}$$

Since there is no reaction or permeation of anions on the surface, the anion flux $\underset{\sim}{\boldsymbol{J}}_-$ satisfies

$$\hat{n} \cdot \underset{\sim}{\boldsymbol{J}}_-\big|_S = 0. \tag{10}$$

The local cation and anion fluxes are related to the local reactive cation concentration $\underset{\sim}{C}_+$, the passive anion concentration $\underset{\sim}{C}_-$, and the electric potential $\underset{\sim}{\Phi}$ by the Nernst-Planck equations,

$$\underset{\sim}{\boldsymbol{J}}_\pm = -\underset{\sim}{\mathcal{D}}_\pm(\underset{\sim}{\boldsymbol{\nabla}}\underset{\sim}{C}_\pm \pm \underset{\sim}{C}_\pm\underset{\sim}{\boldsymbol{\nabla}}\underset{\sim}{\Phi}), \tag{11}$$

where $\underset{\sim}{\mathcal{D}}_\pm = D_\pm/D_{\min}$. These fluxes obey species conservation equations,

$$\underset{\sim}{\boldsymbol{\nabla}} \cdot \underset{\sim}{\boldsymbol{J}}_\pm + \mathrm{Pe}\, \underset{\sim}{\boldsymbol{U}} \cdot \underset{\sim}{\boldsymbol{\nabla}}\underset{\sim}{C}_\pm = 0, \tag{12}$$

where the Péclet number $\mathrm{Pe} = \epsilon\phi_T^2/(\mu D_{\min})$ is the ratio of the characteristic time of diffusion to that of electroviscous flow and determines the significance of convection relative to diffusion in ion migration. At room temperature, $\mathrm{Pe} \simeq 0.05$ for motors operating based on the reaction of hydrogen ions. The potential is uniform on the conductive nanomotor surface and vanishes far from it,

$$\underset{\sim}{\Phi}(\xi = \xi_s) = \underset{\sim}{\phi} < 0, \qquad \underset{\sim}{\Phi}(\xi \to \infty) = 0. \tag{13}$$

Therefore, the asymptotic electro-neutrality condition

$$\underset{\sim}{C}_\pm(\xi \to \infty) = \underset{\sim}{C}_+^\infty \equiv 1 \tag{14}$$

holds far from the motor. The asymmetric ion concentrations $\underset{\sim}{C}_\pm$ and local electric potential $\underset{\sim}{\Phi}$ near the particle are related by the Poisson equation,

$$2\underset{\sim}{\lambda}^2\underset{\sim}{\nabla}^2\underset{\sim}{\Phi} = -(\underset{\sim}{C}_+ - \underset{\sim}{C}_-). \tag{15}$$

The momentum imparted to the fluid by the interaction of the ions with the local electric field $-\underset{\sim}{\boldsymbol{\nabla}}\underset{\sim}{\Phi}$ appears as a body force $-(\underset{\sim}{C}_+ - \underset{\sim}{C}_-)\underset{\sim}{\boldsymbol{\nabla}}\underset{\sim}{\Phi} = \underset{\sim}{\nabla}^2\underset{\sim}{\Phi}\underset{\sim}{\boldsymbol{\nabla}}\underset{\sim}{\Phi}$ in the Stokes equation,

$$\underset{\sim}{\nabla}^2\underset{\sim}{\boldsymbol{U}} + \underset{\sim}{\nabla}^2\underset{\sim}{\Phi}\underset{\sim}{\boldsymbol{\nabla}}\underset{\sim}{\Phi} = \underset{\sim}{\boldsymbol{\nabla}}\underset{\sim}{P}, \tag{16}$$

which together with the continuity equation $\underset{\sim}{\nabla} \cdot \underset{\sim}{\boldsymbol{U}} = 0$ governs the velocity field for low-Reynolds number flow around the motor. The particle moves with speed $\underset{\sim}{\mathcal{U}}$ in the direction $\hat{\mathbf{e}}_z$ (parallel to its symmetry axis from cathode to anode). In the *particle-fixed* frame of reference with a no-slip condition on the particle surface, the fluid velocity obeys

$$\underset{\sim}{\boldsymbol{U}}(\xi = \xi_s) = 0, \qquad \underset{\sim}{\boldsymbol{U}}(\xi \to \infty) = -\underset{\sim}{\mathcal{U}}\,\hat{\mathbf{e}}_z.$$

III. NANOMOTOR VELOCITY

Following earlier analyses for spherical motors,[23,28] we use the method of matched asymptotic expansions to solve for motor speed to leading order in the dimensionless Debye length $\tilde{\lambda}$ and cation flux magnitude $\tilde{j}_+$. As in the recent work on Marangoni propulsion,[46] we work in spheroidal coordinates (in which the Laplace equation is separable) and use the Lorenz reciprocal theorem in conjunction with known results[47] for translation of a spheroid through an otherwise quiescent fluid. To capture the rapid radial variation of electric potential in a thin boundary layer of thickness $O(\tilde{\lambda})$ near the motor surface, the radial coordinate in this inner region is stretched using the transformation,

$$\rho = (\xi - \xi_s)/\tilde{\lambda}.$$

Inner and outer expansions of the form

$$\tilde{G}^i(\rho,\eta) = \sum_{k=n_0}^{\infty} \tilde{\lambda}^k \tilde{G}^{i(k)}(\rho,\eta) \tag{17}$$

and

$$\tilde{G}^o(\xi,\eta) = \sum_{k=0}^{\infty} \tilde{\lambda}^k \tilde{G}^{o(k)}(\xi,\eta), \tag{18}$$

respectively, are then written for each field $\tilde{G}$ and matched to obtain uniform asymptotic expansions. As in earlier analyses for a spherical motor,[23,28] inner expansion (17) begins with $n_0 = -2$ for $\tilde{P}$, $n_0 = -1$ for $\tilde{J}_{\pm\rho}$, $n_0 = 0$ for $\tilde{C}_\pm$, $\tilde{\Phi}$, $\tilde{J}_{\pm\eta}$, and $\tilde{U}_\eta$, and $n_0 = 1$ for $\tilde{U}_\rho$.

The $O(\tilde{\lambda}^0)$ contribution from Poisson Eq. (15) in the outer region gives the electro-neutrality condition,

$$\tilde{C}^{o(0)} \equiv \tilde{C}_+^{o(0)} = \tilde{C}_-^{o(0)}. \tag{19}$$

The $O(\tilde{\lambda}^{-2})$ contribution from species conservation Eq. (12) (i.e., $g_1\partial_\rho \tilde{J}_{\pm\rho}^{i(-1)} = 0$) along with the $O(\tilde{\lambda}^{-1})$ contribution from boundary conditions (8) and (10) leads to $\tilde{J}_{\pm\rho}^{i(-1)} = 0$. This result in conjunction with the $O(\tilde{\lambda}^{-1})$ contribution from Eq. (11), electro-neutrality condition (19), $\tilde{\Phi}^{o(-1)} = 0$, and the matching condition for the radial component of the electric field leads to

$$\tilde{C}_\pm^{i(0)}(\rho,\eta) = \tilde{C}^{o(0)}(\xi_s,\eta)\, \exp\left[\mp\tilde{\psi}^{(0)}(\rho,\eta)\right], \tag{20}$$

where $\tilde{\psi}^{(0)}(\rho,\eta) \equiv \tilde{\Phi}^{i(0)}(\rho,\eta) - \tilde{\Phi}^{o(0)}(\xi_s,\eta)$. Substituting these ion concentrations into the $O(\tilde{\lambda}^0)$ contribution from Poisson Eq. (15) in the inner region subjects to an equipotential surface condition $\tilde{\Phi}^{i(0)}(0,\eta) = \tilde{\phi}^{(0)}$—the leading-order electric potential on the motor surface—and integrating twice yields

$$\tanh\left[\frac{1}{4}\tilde{\psi}^{(0)}(\rho,\eta)\right] = \tanh\left[\frac{1}{4}\tilde{\psi}^{(0)}(0,\eta)\right] \exp\left[-\sqrt{\tilde{C}^{o(0)}(\xi_s,\eta)}\,\frac{\rho}{g_{1,s}(\eta)}\right], \tag{21}$$

where $\tilde{\psi}^{(0)}(0,\eta) = \tilde{\phi}^{(0)} - \tilde{\Phi}^{o(0)}(\xi_s,\eta)$ is the position-dependent potential drop across the inner region, and we have introduced the abbreviation $g_{i,s}(\eta) \equiv g_i(\xi_s,\eta)$ for the metric factors restricted to the surface $\xi = \xi_s$.

To calculate the leading-order slip velocity, $\tilde{\mathbf{U}}_{\text{slip}}^{(0)} = (\lim_{\rho\to\infty} \tilde{U}_\eta^{i(0)})\,\hat{\mathbf{e}}_\eta$, at the outer edge of the inner region, we solve for $\tilde{U}_\eta^{i(0)}$ from the $O(\tilde{\lambda}^{-2})$ part of the η-component of Stokes Eq. (16),

$$(g_{1,s}\partial_\rho)^2 \tilde{U}_\eta^{i(0)} + g_{2,s}\partial_\eta \tilde{\Phi}^{i(0)} (g_{1,s}\partial_\rho)^2 \tilde{\Phi}^{i(0)} = g_{2,s}\partial_\eta \tilde{P}^{i(-2)}, \tag{22}$$

subject to the no-slip boundary condition $\tilde{U}_\eta^{i(0)}(0,\eta) = 0$. Integrating the $O(\tilde{\lambda}^{-3})$ contribution from the radial component of Stokes Eq. (16) and applying the leading-order matching conditions on pressure and the radial component of electric field gives $\tilde{P}^{i(-2)} = \frac{1}{2}\left[g_1\partial_\rho \tilde{\Phi}^{i(0)}\right]^2$. Substituting $\tilde{P}^{i(-2)}$ into Eq. (22), along with Eq. (21), leads to an expression for $\tilde{U}_\eta^{i(0)}$, which in the limit $\rho \to \infty$ yields

the leading-order slip velocity

$$\underset{\sim}{U}^{(0)}_{\text{slip}}(\eta) = \underset{\sim}{\psi}^{(0)}(0,\eta)\, g_{2,s}(\eta)\partial_\eta \underset{\sim}{\Phi}^{o(0)}(\xi_s,\eta) - 4\ln\cosh\left[\frac{\underset{\sim}{\psi}^{(0)}(0,\eta)}{4}\right] g_{2,s}(\eta)\partial_\eta \ln \underset{\sim}{C}^{o(0)}(\xi_s,\eta). \tag{23}$$

We now consider the boundary conditions for ion fluxes in the outer region. The $O(\underset{\sim}{\lambda}^{-1})$ part of species conservation Eq. (12) in the inner region in conjunction with $\underset{\sim}{J}^{i(-1)}_{\pm\rho} = 0$ reduces to $\partial_\rho \underset{\sim}{J}^{i(0)}_{\pm\rho} = 0$. Since $\underset{\sim}{J}^{i(0)}_{\pm\rho}$ does not vary radially in the inner region, applying boundary conditions (8) and (10) and matching the radial components of ion flux result in

$$\underset{\sim}{J}^{i(0)}_{+\rho}(\rho,\eta) = \underset{\sim}{J}^{o(0)}_{+\xi}(\xi_s,\eta) = \underset{\sim}{j}_+ f(\eta), \tag{24a}$$

$$\underset{\sim}{J}^{i(0)}_{-\rho}(\rho,\eta) = \underset{\sim}{J}^{o(0)}_{-\xi}(\xi_s,\eta) = 0, \tag{24b}$$

where the $O(\underset{\sim}{\lambda}^0)$ radial components of flux (from Eq. (11)) in the outer region are

$$\underset{\sim}{J}^{o(0)}_{\pm\xi} = -\underset{\sim}{\mathcal{D}}_\pm \left[g_1 \partial_\xi \underset{\sim}{C}^{o(0)} \pm \underset{\sim}{C}^{o(0)} g_1 \partial_\xi \underset{\sim}{\Phi}^{o(0)} \right]. \tag{25}$$

To leading order in $\underset{\sim}{\lambda}$, both convection-diffusion Eq. (12) and Stokes Eq. (16) are still nonlinear. To proceed with an analytical solution for motor speed, we linearize these equations in the weak field regime by using perturbation expansions in the small parameter $\underset{\sim}{j}_+$ as

$$\underset{\sim}{G}^{o(0)}(\xi,\eta) = \sum_{k=0}^{\infty} \underset{\sim}{j}_+^k \underset{\sim}{G}^{o(0,k)}(\xi,\eta), \tag{26}$$

where $\underset{\sim}{\Phi}^{(0,0)} = \underset{\sim}{U}^{o(0,0)} = \underset{\sim}{\mathcal{U}}^{(0,0)} = 0$, the dimensionless far-field concentration is $\underset{\sim}{C}^{o(0,0)} = \underset{\sim}{C}^{\infty}_{+} = 1$, and $\underset{\sim}{\phi}_0 \equiv \underset{\sim}{\phi}^{(0,0)}$ is the surface potential for an unpowered or uniform-metal ($j_+ = 0$) particle. Writing Eq. (25) to first order in $\underset{\sim}{j}_+$ (namely, $\underset{\sim}{J}^{o(0,1)}_{\pm\xi} = \underset{\sim}{\mathcal{D}}_\pm[g_1\partial_\xi \underset{\sim}{C}^{o(0,1)} \pm g_1 \partial_\xi \underset{\sim}{\Phi}^{o(0,1)}]$) and using the result in the leading-order contributions from convection-diffusion Eqs. (12) and boundary conditions (13), (14), and (24) in the outer region lead to ($\underset{\sim}{G}$ being $\underset{\sim}{C}$ or $\underset{\sim}{\Phi}$)

$$\underset{\sim}{\nabla}^2 \underset{\sim}{G}^{o(0,1)} = 0, \tag{27a}$$

$$\underset{\sim}{G}^{o(0,1)}(\xi \to \infty,\eta) = 0, \tag{27b}$$

$$g_1(\eta)\, \partial_\xi \underset{\sim}{G}^{o(0,1)}(\xi,\eta)\Big|_{\xi=\xi_s} = -\frac{1}{2}\underset{\sim}{\mathcal{D}}_+^{-1} f(\eta). \tag{27c}$$

As mentioned earlier, the Laplace equation is separable in prolate spherical coordinates.[48–50] Using the notation $\{\cdot\}_n$ for the nth Legendre coefficient, i.e., $h(\eta) = \sum_{n=0}^{\infty}\{h\}_n P_n(\eta)$, the solution can be written as

$$\underset{\sim}{C}^{o(0,1)}(\xi,\eta) = \underset{\sim}{\Phi}^{o(0,1)}(\xi,\eta) = -\frac{\varepsilon}{2\underset{\sim}{\mathcal{D}}_+} \sum_{n=1}^{\infty} \frac{1}{Q_n'(\varepsilon^{-1})} \left\{ \frac{f}{\varepsilon g_{1,s}} \right\}_n Q_n(\xi) P_n(\eta), \tag{28}$$

where P_n and Q_n are Legendre functions of first and second kinds, respectively, and $\{f/(\varepsilon g_{1,s})\}_0 = 0$ because of the zero net flux condition imposed by Eq. (9). We recall that the Legendre functions $Q_n(\xi)$ can be expressed as (second form for $n > 0$)

$$Q_0(\xi) = \frac{1}{2}\ln\frac{\xi+1}{\xi-1}, \quad Q_n(\xi) = P_n(\xi)Q_0(\xi) - \sum_{\substack{0\le k<n \\ k\not\equiv n \pmod 2}} \frac{2(2k+1)P_k(\xi)}{(n+k+1)(n-k)}, \tag{29}$$

and the derivative in (28) can be obtained from the recurrence relation $(1-\xi^2)Q_n'(\xi) = n[Q_{n-1}(\xi) - \xi Q_n(\xi)]$ for $n \ge 1$.

To determine the leading-order swimming speed, we solve the Stokes and continuity equations at $O(\underset{\sim}{\lambda}^0, \underset{\sim}{j}_+)$ in the *laboratory-fixed* frame of reference, i.e.,

$$\underset{\sim}{\nabla}^2 \underset{\sim}{\boldsymbol{U}}^{o(0,1)} = \underset{\sim}{\boldsymbol{\nabla}} \underset{\sim}{P}^{o(0,1)}, \tag{30a}$$

$$\underset{\sim}{\boldsymbol{\nabla}} \cdot \underset{\sim}{\boldsymbol{U}}^{o(0,1)} = 0, \tag{30b}$$

subject to the far-field conditions,

$$\underset{\sim}{P}^{o(0,1)}(\xi \to \infty,\eta) = 0, \tag{31}$$

$$\underset{\sim}{\boldsymbol{U}}^{o(0,1)}(\xi \to \infty, \eta) = 0 \tag{32}$$

and the slip condition,

$$\underset{\sim}{\boldsymbol{U}}^{o(0,1)}(\xi_s, \eta) = \underset{\sim}{U}_{\text{slip}}^{(0,1)}\,\hat{\mathbf{e}}_\eta + \underset{\sim}{\mathcal{U}}^{(0,1)}\,\hat{\mathbf{e}}_z, \tag{33}$$

at the particle surface. The leading-order slip velocity on the right-hand side (RHS) of (33) is given by the $O(\underset{\sim}{\lambda}^0, \underset{\sim}{j}_+)$ contribution from Eq. (23), which using $\underset{\sim}{\zeta}^{o(0,1)} = \underset{\sim}{\Phi}^{o(0,1)}$ from (28) and the identity $\ln(1+\tanh\zeta) = \zeta - \ln\cosh\zeta$ reduces to

$$\underset{\sim}{U}_{\text{slip}}^{(0,1)} = 4\ln\left[1 + \tanh\frac{\underset{\sim}{\phi}_0}{4}\right] g_{2,s}(\eta)\,\partial_\eta \underset{\sim}{\Phi}^{o(0,1)}(\xi_s, \eta). \tag{34}$$

Although electroneutrality at $O(\underset{\sim}{\lambda}^0)$ in the outer region causes the body force term to be absent in the leading-order contribution to the Stokes equation, the electrokinetic effect of electric potential manifests itself through the slip velocity [Eq. (34)] appearing in boundary condition (33) at the motor surface.

Noting that the far-field velocity vanishes in the laboratory-fixed frame [cf. Eq. (32)], the unknown particle velocity $\underset{\sim}{\mathcal{U}}^{(0,1)}$ in Eq. (33) can be determined by applying the Lorentz reciprocal theorem for low Reynolds number flow,[51–53]

$$\int_S \hat{n}\cdot\underset{\sim}{\mathbb{T}}^{o(0,1)}\cdot\underset{\sim}{\boldsymbol{U}}'\,\mathrm{d}\underset{\sim}{A} = \int_S \hat{n}\cdot\underset{\sim}{\mathbb{T}}'\cdot\underset{\sim}{\boldsymbol{U}}^{o(0,1)}\,\mathrm{d}\underset{\sim}{A}, \tag{35}$$

where $\underset{\sim}{\mathbb{T}}^{o(0,1)}$ is the Newtonian stress tensor corresponding to the $O(\underset{\sim}{\lambda}^0, \underset{\sim}{j}_+)$ flow problem. Also, $\underset{\sim}{\boldsymbol{U}}'$ and $\underset{\sim}{\mathbb{T}}'$ are selected to be the velocity and Newtonian stress distributions for steady translation of a spheroid with velocity $\underset{\sim}{\boldsymbol{\mathcal{U}}}' = \hat{\mathbf{e}}_z$ along its symmetry axis in an otherwise quiescent fluid, for which the surface traction distribution is known to be $\hat{n}\cdot\underset{\sim}{\mathbb{T}}' \propto g_{1,s}(\eta)\,\hat{\mathbf{e}}_z$.[47] Since the particle is force-free, the left-hand side of Eq. (35) vanishes; working out the right-hand side then yields

$$\underset{\sim}{\mathcal{U}}^{(0,1)} = -2\ln\left[1 + \tanh\frac{\underset{\sim}{\phi}_0}{4}\right]\int_{-1}^{1}\partial_\eta\underset{\sim}{\Phi}^{o(0,1)}(\xi_s,\eta)g_{2,s}^2(\eta)d\eta. \tag{36}$$

Substituting Eq. (28) for $\underset{\sim}{\Phi}^{o(0,1)}(\xi_s,\eta)$ into this expression leads to the final general expression for the dimensional speed of a prolate spheroidal electrocatalytic motor,

$$\mathcal{U} = -\left(\frac{2\lambda_D^2\phi_T z F}{\mu D_+}\right)\ln\left[1+\tanh\frac{\phi_0}{4\phi_T}\right]\sum_{n=1}^{\infty} w_n(\varepsilon)\left\{\frac{\hat{n}\cdot\boldsymbol{J}_+}{\varepsilon g_{1,s}(\eta)}\right\}_n, \tag{37}$$

where

$$w_n(\varepsilon) = -\frac{\varepsilon Q_n(\varepsilon^{-1})}{Q_n'(\varepsilon^{-1})}\int_{-1}^{1} g_{2,s}^2(\eta)P_n'(\eta)d\eta = -\frac{2\varepsilon Q_n(\varepsilon^{-1})}{(1-\varepsilon^2)Q_n'(\varepsilon^{-1})}\int_{-1}^{1}\left[\varepsilon g_{1,s}(\eta)\right]^4\eta P_n(\eta)d\eta \tag{38}$$

depend only on the shape (eccentricity) of the motor, which we have emphasized through the notation, and the Legendre coefficients

$$\left\{\frac{\hat{n}\cdot\boldsymbol{J}_+}{\varepsilon g_{1,s}(\eta)}\right\}_n = \frac{(2n+1)}{4\pi(1-\varepsilon^2)}\int_A \hat{n}\cdot\boldsymbol{J}_+\,P_n(\eta)\,d\underset{\sim}{A} \tag{39}$$

extract information on the distribution of the surface cation flux. They are proportional to the weighted surface average of cation flux, with the contribution of the surface cation flux weighted more heavily near the two ends of the spheroid where the Legendre polynomial weights attain their largest absolute values over the interval $[-1,1]$. In addition, since the integrand in (38) is an odd function of η for even Legendre polynomials, the integral vanishes for even values of n and the sum in (37) reduces to one over odd values of n. The parenthesized prefactor in Eq. (37) depends on the properties of the solution in which the motor operates through λ_D, μ, and D_+. Its dependence on the motor operation is only through the identity of the reactive cation. Detailed dependence on the characteristics of the motor therefore enters only through j_+, ϕ_0, and $f(\eta)$. Note that the *size* of the motor, a, does not appear in (37). This is not, however, to say that motor speed is independent of size under the natural conditions of fixed fuel concentration, since j_+, ϕ_0, and $f(\eta)$ may well have hidden

size dependence which is beyond the scope of our theory to calculate *a priori*. This is investigated in Sec. IV.

In the spherical limit $\varepsilon \to 0$, $\varepsilon g_{1,s}(\eta) \sim 1$ so that $w_n \sim \frac{2}{3}\delta_{1n}$ (as shown in the Appendix) and the summation in Eq. (37) reduces to $\frac{2}{3}\{\hat{n}\cdot \boldsymbol{J}_+\}_1$, which is identical to our earlier result for a spherical motor reported in Ref. 23. In the rod-like limit $\varepsilon \to 1$, Eq. (37) leads to a vanishing motor speed that is asymptotically consistent with the prediction of Yariv's slender-body analysis,[28] as shown in the Appendix. A variety of axisymmetric motor geometries can be considered by changing the fraction of the motor surface that acts as a source of cations, as characterized by the cap $\eta > \eta_0$ in Fig. 2. For a piecewise-uniform surface cation flux distribution of the form

$$\hat{n}\cdot \underset{\sim}{\boldsymbol{J}}_+\big|_S = \underset{\sim}{j}_+ f(\eta) = \underset{\sim}{j}_+ \begin{cases} f_+ & \text{if } \eta > \eta_0 \\ -f_- & \text{if } \eta < \eta_0 \end{cases}, \tag{40}$$

the constraints imposed by Eq. (9) on the net surface flux of cations yield

$$f_+ = \frac{1}{2\beta}, \qquad f_- = \frac{1}{2(1-\beta)}, \tag{41}$$

where

$$\beta = \frac{1}{2}\left[1 - \frac{\varepsilon\eta_0\sqrt{1-\varepsilon^2\eta_0^2} + \sin^{-1}(\varepsilon\eta_0)}{\varepsilon\sqrt{1-\varepsilon^2} + \sin^{-1}\varepsilon}\right] \tag{42}$$

is the fraction of the motor surface that acts as a source of cations. The motor speed resulting from Eq. (37) for the special case of a piecewise-uniform cation flux distribution can then be written as

$$\frac{\mathcal{U}}{\mathcal{U}_0} := \frac{3}{2\{f\}_1\big|_{\varepsilon=0}} \sum_{n\ \text{odd}} w_n(\varepsilon)\left\{\frac{f(\eta)}{\varepsilon g_{1,s}}\right\}_n = \sum_{n\ \text{odd}} w_n(\varepsilon)\left\{\frac{f(\eta)}{\varepsilon g_{1,s}}\right\}_n, \tag{43}$$

where $\mathcal{U}_0 = \mathcal{U}(\varepsilon = 0)$ is the corresponding speed of a spherical motor with the same characteristics (i.e., j_+, ϕ_0, and β).

The effect of eccentricity on relative mobility $\frac{\mathcal{U}}{\mathcal{U}_0}$ of prolate spheroidal motors with piecewise-uniform surface cation flux distribution is shown in Fig. 3. For a symmetric surface cation flux distribution ($\eta_0 = 0$) represented by the dotted curve in Fig. 3, the relative mobility decreases monotonically with increasing eccentricity, as the shape of the spheroid changes from spherical to rod-like by reducing the minor radius while keeping the major radius fixed. The size of the cation source cap $\eta > \eta_0$ can be varied from a symmetric design by increasing $|\eta_0|$, noting that relative mobility is an even function of η_0. For asymmetric cation source/sink configurations, the speed of a spherical motor does not change (as was also reported in Ref. 23). For $\varepsilon > 0$, however, prolate spheroidal motors with asymmetric cation source/sink configurations move faster than their symmetric counterparts, with their relative mobility monotonically increasing with $|\eta_0|$ characterizing the extent of asymmetry. Using (40) in (43), the asymptotic behavior of $\frac{\mathcal{U}}{\mathcal{U}_0}$ for small ε is found to be

$$\frac{\mathcal{U}}{\mathcal{U}_0} \sim 1 + \frac{1}{12}\varepsilon^2(7\eta_0^2 - 3) + O(\varepsilon^4) \quad \text{as} \quad \varepsilon \to 0. \tag{44}$$

Hence, the dependence of relative mobility on eccentricity for nearly spherical motors has an inflection point at $|\eta_0| = (3/7)^{1/2} \simeq 0.655$. For $|\eta_0| < 0.655$, the relative mobility remains a monotonically decreasing function of eccentricity so that a prolate spheroidal motor moves slower than a spherical motor with the same major radius regardless of the cation source/sink configuration. For $|\eta_0| > 0.655$, on the other hand, the relative mobility initially increases as the eccentricity of a prolate spheroidal motor increases and reaches a maximum before rapidly decreasing with further increase in eccentricity for rod-like motors. It is interesting to note that as the asymmetry in the source/sink configuration increases, the motor shape for which maximum motor speed is achieved approaches the prolate spheroidal shape of fixed surface area that minimizes drag in uniform axial flow, which is characterized by an eccentricity value of $\varepsilon \simeq 0.97$. For fixed j_+, a prolate spheroidal motor with $\varepsilon \simeq 0.9$ and a highly asymmetrical cation source/sink configuration ($|\eta_0 = 0.9|$) are predicted to

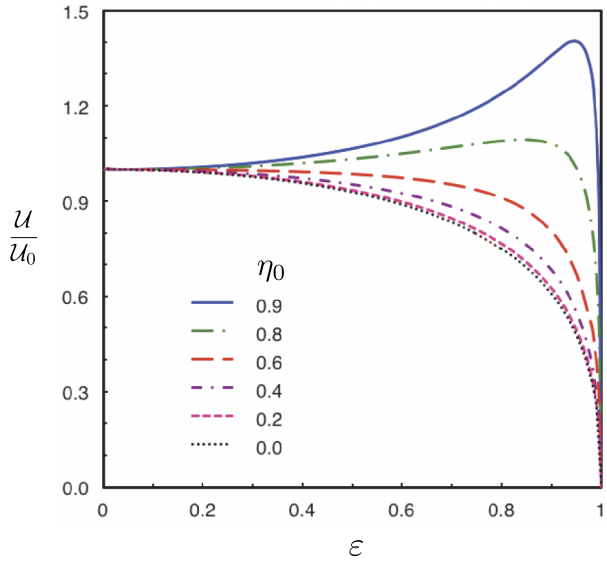

FIG. 3. Effect of eccentricity on relative mobility of spheroidal motors with a piecewise uniform distribution of surface cation flux and a cation source characterized by the cap $\eta > \eta_0$. $\mathcal{U}_0 = \mathcal{U}(\varepsilon = 0)$ is the corresponding speed of a spherical motor characterized with the same values of j_+, ϕ_0, and β.

move about three times faster than its symmetrical counterpart and about 40% faster than a spherical motor with the same characteristics.

IV. COMPARISON TO EXPERIMENTS

In this section, we apply Eq. (37) to the experimental data of Dhar *et al.*,[54] who measured speeds for a series of Au/Pt rods of various lengths in 3.3% hydrogen peroxide solution. The data analyzed here are those for 1:1 Pt/Au rods in Table 1 of their paper. We calculate $-j_+ \ln\left[1 + \tanh\frac{\phi_0}{4\phi_T}\right]$ from Eq. (37) under the simplifying assumption that $f(\eta)$ has constant absolute value everywhere on the rod, with one sign on the Au end and the opposite sign on the Pt end. Making a spheroidal approximation to a cylinder by matching the cylinder length to $2a$ and its diameter to $2b$, we solve for $-j_+ \ln\left[1 + \tanh\frac{\phi_0}{4\phi_T}\right]$ using the measured speeds. The results are depicted in Figure 4. Both j_+ and ϕ_0 are influenced by the chemical kinetics and the concentration of hydrogen peroxide. In the linear response regime for Frumkin-Butler-Volmer kinetics of first order in hydrogen ion and hydrogen peroxide concentrations, $\phi_0 \sim O(\phi_T)$ is independent of peroxide concentration,[24,29] and the speed of a spherical motor of radius r scales as

$$\mathcal{U}_{\text{sphere}} \propto \frac{J_{\text{exch}}}{1 + \frac{r}{2} J_{\text{exch}}/(D_+ C_+^\infty)}, \tag{45}$$

where the exchange flux J_{exch} addresses the majority of production and consumption of hydrogen ions over the motor surface. We can assign a length scale ℓ associated with the radial motion of ions from the surface such that the surface production of hydrogen ion is equal to its flux across that length scale, i.e., $J_{\text{exch}} = D_+ C_+^\infty/\ell$. Since $\mathcal{U} \propto j_+$ for a spherical geometry, we consider the ansatz

$$j_+ = \frac{j_+^*}{1 + \frac{a}{2\ell}}. \tag{46}$$

Assuming $\phi_0 \simeq -40$ mV, this may now be fit to the experimental data, as shown by the solid curve in Fig. 4, to yield $\ell = 2.4$ μm and $j_+^* = 2.4 \times 10^{-6}$ mol $\cdot$ m$^{-2} \cdot$ s^{-1}. Removing the data point for the motor with $2a = 6$ μm from the fit leads to values of $\ell = 1.2$ μm and $j_+^* = 2.9 \times 10^{-6}$ mol $\cdot$ m$^{-2} \cdot$ s^{-1} for the dashed curve in Fig. 4. The resulting value for the length scale is reasonable, but that for j_+^* is on the order of 10% of the total peroxide decomposition rate on Au-Pt rods (as determined

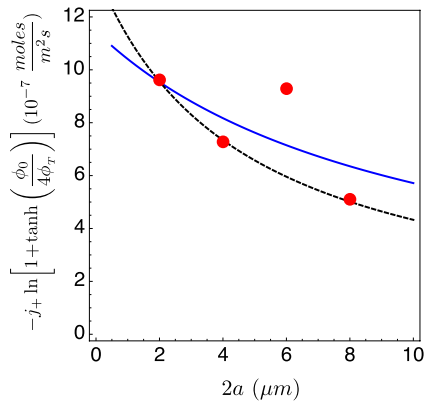

FIG. 4. The magnitude of the surface cation flux j_+ vs. rod length ℓ. The experimental data are obtained from Table 1 of Ref. 54 and j_+ is calculated using Eq. (37).

by oxygen evolution measurements[27]), compared to estimates of about 1% for the electrochemical fraction.

V. DISCUSSION AND CONCLUSION

For simplicity, we have assumed a symmetric binary electrolyte in the analysis presented here. In practical situations, addition of chemically inert salt may be of interest. In the *linear* regime, for given surface cation flux distribution $\hat{n}\cdot\boldsymbol{J}_+$ and interfacial potential ϕ_0, the presence of such salt in the electrolyte affects only the thickness of the diffuse layer. We offer two approaches to assessing the consequences of extra salt, while avoiding unnecessary complications in the formulation and analytical solution. One frequently used assumption is that all ionic valences have the same absolute value[29] and the diffusivities of all ions are the same.[28,29] In that case, we can sum concentration fields of reactive and salt cations into a net cation concentration field and similarly sum the anion concentration fields, thus turning the system into an effective binary symmetric electrolyte. The second approach eliminates C^{∞}_{salt} from Debye length (1), solves the problem in the absence of salt while assuming that the diffusivities of anions and cations are different, and then returns C^{∞}_{salt} to the Debye length in the final expression to include the effect of salt in the thickness of diffuse layer. Within the scope of this problem, both methods give similar mathematical formulations and the same result.

Electrocatalytic nanomotors can be fabricated in a great variety and complication of shapes. There is little hope that tractable formulas for the motor speed can be obtained without resorting to laborious numerical computations. Indeed, we suspect that Eq. (37) for prolate spheroids represents nearly the practical limit. Oblate spheroids could also probably be treated, but are likely of less practical interest.

ACKNOWLEDGMENTS

This work was supported by the National Science Foundation under Grant Nos. DMR-0820404 and DMR-1420620 through the Penn State Center for Nanoscale Science. We thank Tom Mallouk for clarification about Reference 54.

APPENDIX: ASYMPTOTIC LIMITS FOR SPHERICAL AND ROD-LIKE MOTORS

The asymptotic forms of Eq. (37) for motor speed in the spherical ($\varepsilon \to 0$) and rod-like ($\varepsilon \to 1$) limits are examined in this section. The shape factors $w_n(\varepsilon)$ given by Eq. (38) can be written explicitly in terms of eccentricity as

$$w_n(\varepsilon) = -\frac{\varepsilon Q_n(\varepsilon^{-1})}{Q'_n(\varepsilon^{-1})}\int_{-1}^{1}\left(\frac{1-\eta^2}{1-\varepsilon^2\eta^2}\right)P'_n(\eta)d\eta = \frac{-2\varepsilon(1-\varepsilon^2)Q_n(\varepsilon^{-1})}{Q'_n(\varepsilon^{-1})}\int_{-1}^{1}\frac{\eta P_n(\eta)}{(1-\varepsilon^2\eta^2)^2}d\eta. \tag{A1}$$

Using an integral representation of the Legendre functions Q_n and simplifying the result for odd n yield

$$Q_n(x) = \frac{1}{2}\int_{-1}^{1} \frac{P_n(t)}{(x-t)}\,dt = \frac{1}{2}\int_0^1 \left(\frac{1}{x-t} - \frac{1}{x+t}\right) P_n(t)\,dt = \int_0^1 \frac{tP_n(t)}{(x^2-t^2)}\,dt \quad \text{for odd n,} \tag{A2}$$

so that $Q_n(\varepsilon^{-1})$ appearing in Eq. (A1) can be written as

$$Q_n(\varepsilon^{-1}) = \varepsilon^2 \int_0^1 \frac{\eta P_n(\eta)}{(1-\varepsilon^2\eta^2)}\,d\eta \quad \text{for n odd.} \tag{A3}$$

It can be readily shown from this expression that $Q_1(\varepsilon^{-1}) \sim \varepsilon^2/3$ and $Q_1'(\varepsilon^{-1}) \sim -2\varepsilon^3/3$ in the spherical limit $\varepsilon \to 0$. Hence, Eq. (A1) yields $w_n \sim \frac{2}{3}\delta_{1n}$ as $\varepsilon \to 0$, and the summation in Eq. (37) reduces to $\frac{2}{3}\{\hat{n}\cdot\boldsymbol{J}_+\}_1$, which is identical to our earlier result for a spherical motor.[23]

In the rod-like limit $\varepsilon \to 1$, the asymptotic behavior of w_n resulting from Eq. (A1) is

$$w_n(\varepsilon) \sim -2\lim_{\varepsilon\to 1}\frac{\varepsilon Q_n(\varepsilon^{-1})}{Q_n'(\varepsilon^{-1})} \sim \lim_{\varepsilon\to 1} 2(1-\varepsilon^2)\int_0^1 \frac{\eta P_n(\eta)}{(1-\varepsilon^2\eta^2)}\,d\eta \sim \lim_{\varepsilon\to 1}\frac{2(1-\varepsilon^2)}{(2n+1)}\left\{\frac{\eta}{(1-\varepsilon^2\eta^2)}\right\}_n. \tag{A4}$$

Hence, the summation on the right-hand side of Eq. (37) for motor speed asymptotically reduces as follows:

$$\begin{aligned}
\lim_{\varepsilon\to 1}\sum_{n=1}^{\infty} w_n(\varepsilon)\left\{\frac{\hat{n}\cdot\boldsymbol{J}_+}{\varepsilon g_{1,s}(\eta)}\right\}_n &\sim (1-\varepsilon^2)^{1/2}\lim_{\varepsilon\to 1}\sum_{n=1}^{\infty}\frac{2}{(2n+1)}\left\{\frac{\eta}{(1-\varepsilon^2\eta^2)}\right\}_n\left\{(\hat{n}\cdot\boldsymbol{J}_+)(1-\varepsilon^2\eta^2)^{1/2}\right\}_n \\
&\sim (1-\varepsilon^2)^{1/2}\lim_{\varepsilon\to 1}\sum_{n=1}^{\infty}\left\{(\hat{n}\cdot\boldsymbol{J}_+)(1-\varepsilon^2\eta^2)^{1/2}\right\}_n\sum_{k=1}^{\infty}\left\{\frac{\eta}{(1-\varepsilon^2\eta^2)}\right\}_k\int_{-1}^{1}P_n(\xi)P_k(\xi)\,d\xi \\
&\sim (1-\varepsilon^2)^{1/2}\lim_{\varepsilon\to 1}\int_{-1}^{1}\left[\sum_{n=1}^{\infty}\left\{(\hat{n}\cdot\boldsymbol{J}_+)(1-\varepsilon^2\eta^2)^{1/2}\right\}_n P_n(\xi)\right]\left[\sum_{k=1}^{\infty}\left\{\frac{\eta}{(1-\varepsilon^2\eta^2)}\right\}_k P_k(\xi)\right]d\xi \\
&\sim (1-\varepsilon^2)^{1/2}\lim_{\varepsilon\to 1}\int_{-1}^{1}\left(\frac{\eta}{1-\varepsilon^2\eta^2}\right)(\hat{n}\cdot\boldsymbol{J}_+)(1-\varepsilon^2\eta^2)^{1/2}\,d\eta \\
&\sim -(1-\varepsilon^2)^{1/2}\int_{-1}^{1}(\hat{n}\cdot\boldsymbol{J}_+)\frac{d}{d\eta}(1-\eta^2)^{1/2}\,d\eta\,.
\end{aligned} \tag{A5}$$

This is consistent with the result of Yariv's slender-body analysis[28] and predicts a vanishing motor speed in the limit $\varepsilon \to 1$.

[1] W. Wang, W. Duan, S. Ahmed, T. E. Mallouk, and A. Sen, "Small power: Autonomous nano- and micromotors propelled by self-generated gradients," Nano Today **8**, 531 (2013).
[2] G. A. Ozin, "Channel crossing by a catalytic nanomotor," ChemCatChem **5**, 2798 (2013).
[3] W. Gao and J. Wang, "The environmental impact of micro/nanomachines: A review," ACS Nano **8**, 3170 (2014).
[4] A. Nourhani, P. E. Lammert, A. Borhan, and V. H. Crespi, "Chiral diffusion of rotary nanomotors," Phys. Rev. E **87**, 050301(R) (2013).
[5] A. Nourhani, P. E. Lammert, A. Borhan, and V. H. Crespi, "Kinematic matrix theory and universalities in self-propellers and active swimmers," Phys. Rev. E **89**, 062304 (2014).
[6] A. Nourhani, V. H. Crespi, and P. E. Lammert, "Gaussian memory in kinematic matrix theory for self-propellers," Phys. Rev. E **90**, 062304 (2014).
[7] R. Golestanian, T. B. Liverpool, and A. Ajdari, "Propulsion of a molecular machine by asymmetric distribution of reaction products," Phys. Rev. Lett. **94**, 220801 (2005).
[8] R. Golestanian, T. B. Liverpool, and A. Ajdari, "Designing phoretic micro-and nano-swimmers," New J. Phys. **9**, 126 (2007).
[9] J. R. Howse, R. A. L. Jones, A. J. Ryan, T. Gough, R. Vafabakhsh, and R. Golestanian, "Self-motile colloidal particles: From directed propulsion to random walk," Phys. Rev. Lett. **99**, 048102 (2007).
[10] S. Sengupta, M. E. Ibele, and A. Sen, "Fantastic voyage: Designing self-powered nanorobots," Angew. Chem., Int. Ed. **51**, 8434 (2012).
[11] T. Mirkovic, N. S. Zacharia, G. D. Scholes, and G. A. Ozin, "Nanolocomotion-catalytic nanomotors and nanorotors," Small **6**, 159 (2010).
[12] S. J. Ebbens and J. R. Howse, "In pursuit of propulsion at the nanoscale," Soft Matter **6**, 726 (2010).
[13] J. Wang and K. M. Manesh, "Motion control at the nanoscale," Small **6**, 338 (2010).
[14] T. Mirkovic, N. S. Zacharia, G. D. Scholes, and G. A. Ozin, "Fuel for thought: Chemically powered nanomotors out-swim nature's flagellated bacteria," ACS Nano **4**, 1782 (2010).

[15] J. Wang, "Can man-made nanomachines compete with nature biomotors?," ACS Nano **3**, 4 (2009).
[16] W. F. Paxton, S. Sundararajan, T. E. Mallouk, and A. Sen, "Chemical locomotion," Angew. Chem., Int. Ed. **45**, 5420 (2006).
[17] H. H. Kung and M. C. Kung, "Catalytic nanomotors—Promising leads for new catalytic applications," Appl. Catal., A: Gen. **309**, 159 (2006).
[18] R. Dreyfus, J. Baudry, M. L. Roper, M. Fermigier, H. A. Stone, and J. Bibette, "Microscopic artificial swimmers," Nature **437**, 862 (2005).
[19] W. F. Paxton, A. Sen, and T. E. Mallouk, "Motility of catalytic nanoparticles through self-generated forces," Chem. - Eur. J. **11**, 6462 (2005).
[20] G. A. Ozin, I. Manners, S. Fournier-Bidoz, and A. Arsenault, "Dream nanomachines," Adv. Mater. **17**, 3011 (2005).
[21] W. F. Paxton, K. C. Kistler, C. C. Olmeda, A. Sen, S. K. St Angelo, Y. Y. Cao, T. E. Mallouk, P. E. Lammert, and V. H. Crespi, "Catalytic nanomotors: Autonomous movement of striped nanorods," J. Am. Chem. Soc. **126**, 13424 (2004).
[22] S. Fournier-Bidoz, A. C. Arsenault, I. Manners, and G. A. Ozin, "Synthetic self-propelled nanorotors," Chem. Commun. **2005**, 441.
[23] A. Nourhani, P. E. Lammert, V. H. Crespi, and A. Borhan, "A general flux-based analysis for spherical electrocatalytic nanomotors," Phys. Fluids. **27**, 012001 (2015).
[24] A. Nourhani, V. H. Crespi, and P. E. Lammert, "Self-consistent nonlocal feedback theory for electrocatalytic swimmers with heterogeneous surface chemical kinetics," Phys. Rev. E **91**, 062303 (2015).
[25] A. Nourhani, P. E. Lammert, A. Borhan, and V. H. Crespi, "Nanomotor mechanisms and motive force distributions from nanorotor trajectories," Phys. Rev. E **88**, 062317 (2013).
[26] Y. Wang, R. M. Hernandez, D. J. Bartlett, J. M. Bingham, T. R. Kline, A. Sen, and T. E. Mallouk, "Bipolar electrochemical mechanism for the propulsion of catalytic nanomotors in hydrogen peroxide solutions," Langmuir **22**, 10451 (2006).
[27] W. F. Paxton, P. T. Baker, T. R. Kline, Y. Wang, T. E. Mallouk, and A. Sen, "Catalytically induced electrokinetics for motors and micropumps," J. Am. Chem. Soc. **128**, 14881 (2006).
[28] E. Yariv, "Electrokinetic self-propulsion by inhomogeneous surface kinetics," Proc. R. Soc. A: Math., Phys. Eng. Sci. **467**, 1645 (2011).
[29] B. Sabass and U. Seifert, "Nonlinear, electrocatalytic swimming in the presence of salt," J. Chem. Phys. **136**, 214507 (2012).
[30] W. Wang, T.-Y. Chiang, D. Velegol, and T. E. Mallouk, "Understanding the efficiency of autonomous nano- and microscale motors," J. Am. Chem. Soc. **135**, 10557 (2013).
[31] J. Moran, P. Wheat, and J. Posner, "Locomotion of electrocatalytic nanomotors due to reaction induced charge autoelectrophoresis," Phys. Rev. E **81**, 065302 (2010).
[32] R. Laocharoensuk, J. Burdick, and J. Wang, "Carbon-nanotuble-induced acceleration of catalytic nanomotors," ACS Nano **2**, 1069 (2008).
[33] U. K. Demirok, R. Laocharoensuk, K. M. Manesh, and J. Wang, "Ultrafast catalytic alloy nanomotors," Angew. Chem., Int. Ed. **47**, 9349 (2008).
[34] N. S. Zacharia, Z. S. Sadeq, and G. A. Ozin, "Enhanced speed of bimetallic nanorod motors by surface roughening," Chem. Commun. 5856 (2009).
[35] T. R. Kline, W. F. Paxton, T. E. Mallouk, and A. Sen, "Catalytic nanomotors: Remote-controlled autonomous movement of striped metallic nanorods," Angew. Chem., Int. Ed. **44**, 744 (2005).
[36] J. Burdick, R. Laocharoensuk, P. M. Wheat, J. D. Posner, and J. Wang, "Synthetic nanomotors in microchannel networks: Directional microchip motion and controlled manipulation of cargo," J. Am. Chem. Soc. **130**, 8164 (2008).
[37] S. Sundararajan, P. E. Lammert, A. W. Zudans, V. H. Crespi, and A. Sen, "Catalytic motors for transport of colloidal cargo," Nano Lett. **8**, 1271 (2008).
[38] J. L. Moran and J. D. Posner, "Electrokinetic locomotion by reaction induced charge auto-electrophoresis," J. Fluid Mech. **680**, 31 (2011).
[39] D. A. Saville, "Electrokinetic effects with small particles," Annu. Rev. Fluid Mech. **9**, 321 (1977).
[40] R. A. Rica and M. Z. Bazant, "Electrodiffusiophoresis: Particle motion in electrolytes under direct current," Phys. Fluids **22**, 112109 (2010).
[41] E. Yariv, "Migration of ion-exchange particles driven by a uniform electric field," J. Fluid Mech. **655**, 105 (2010).
[42] E. Yariv, "Boundary-induced electrophoresis of uncharged conducting particles: Remote wall approximations," Proc. R. Soc. A **465**, 709 (2009).
[43] O. Schnitzer and E. Yariv, "Induced-charge electro-osmosis beyond weak fields," Phys. Rev. E **86**, 061506 (2012).
[44] Y. Ben, E. A. Demekhin, and H.-C. Chang, "Nonlinear electrokinetics and superfast electrophoresis," J. Colloid Interface Sci. **276**, 483 (2004).
[45] B. Zaltzman and I. Rubinstein, "Electro-osmotic slip and electroconvective instability," J. Fluid Mech. **579**, 173 (2007).
[46] H. Masoud and H. A. Stone, "A reciprocal theorem for Marangoni propulsion," J. Fluid Mech. **741**, R4 (2014).
[47] H. Brenner, "The Stokes resistance of an arbitrary particle: Arbitrary fields of flow," Chem. Eng. Sci. **19**, 703 (1964).
[48] D. Zwillinger, *CRC Standard Mathematical Tables and Formulae*, 31st ed. (JChapman & Hall/CRC, New York, 2003).
[49] N. M. Temme, *Special Functions and an Introduction to the Classical Functions of Mathematical Physics* (John Wiley & Sons, Inc., New York, 1996).
[50] N. N. Lebedev, *Special Functions and their Applications*, unabridged and corrected republication, revised edition, translated from the Russian and edited by R. A. Silverman (Dover Publications, Inc., New York, 1972).
[51] J. Happel and H. Brenner, *Low Reynolds Number Hydrodynamics* (Springer, New York, NY, 1983).
[52] L. G. Leal, *Advanced Transport Phenomena: Fluid Mechanics and Convective Transport Processes* (Cambridge University Press, New York, 2007).
[53] S. Kim and S. J. Karrila, *Microhydrodynamics: Principles and Selected Applications* (Dover Publications, 2005).
[54] P. Dhar, Th. M. Fischer, Y. Wang, T. E. Mallouk, W. F. Paxton, and A. Sen, "Autonomously moving nanorods at a viscous interface," Nano Lett. **6**, 66 (2006).